Supplementary Information for

Reduced Auger recombination in single CdSe/CdS nanorods by one-dimensional electron delocalization

Freddy T. Rabouw,[1] Per Lunnemann,[2,*] Relinde J. A. van Dijk-Moes,[1] Martin Frimmer,[2,†] Francesca Pietra,[1] A. Femius Koenderink,[2] and Daniël Vanmaekelbergh[1,‡]

[1] *Condensed Matter and Interfaces, Debye Institute for Nanomaterials Science, Princetonplein 1, 3584 CC Utrecht, The Netherlands*
[2] *Center for Nanophotonics, FOM Institute AMOLF, Science Park 104, 1098 XG Amsterdam, The Netherlands*

* Current address: DTU Fotonik, Department of Photonics Engineering, Technical University of Denmark, DK-2800 Kongens Lyngby, Denmark
† Current address: Photonics Laboratory, ETH Zürich, 8093 Zürich, Switzerland
‡ d.vanmaekelbergh@uu.nl

TABLE OF CONTENTS

- Figure S1 | Demonstration that the characteristics extracted for the grey state B are robust to more conversative assumptions than used in the main text.
- Figure S2 | Proposal of a ternary nanocrystal in which the band alignment results in partial delocalization for both electron and hole, potentially leading to reduced Auger recombination in all excitonic states.
- Supplementary Discussion 1 | Discussion of the presence of quenching of biexciton emission, including the experimental evidence, and a short description of the mechanism.
- Supplementary Discussion 2 | Discussion of the two methods used to estimate radiative and non-radiative decay contributions from the fit results. We discuss the assumptions made, and rationalize why the two methods yield slightly different results.
- Supplementary Discussion 3 | Discussion of the transition energies, including a qualitative rationalization of the differences in transition energy between the neutral and charged exciton states, and a comparison to previous literature reports.
- Supplementary Methods | Decription of the quantum-mechanical effective-mass calculations used to predict transition energies and radiative lifetimes of the neutral and charged exciton states.
- Supplementary Data | Overview of the experimental results of the 18 single NRs examined: the photon-photon correlation, the fluorescence-lifetime-intensity-distribution, the emission-wavelength-intensity-distribution, and the state-averaged PL decay curves and emission spectra.

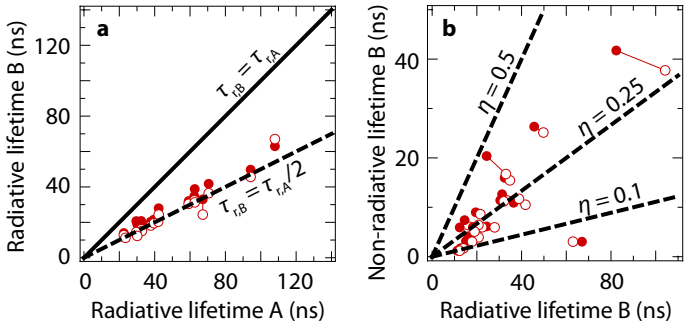

Figure S1 | Overview of the characteristics of the grey state B for 18 single NRs, under the conservative assumptions that $\eta_A = 0.75$ and 20% lower excitation rate of state B compared to state A. Estimates obtained by method 1 (via the photon count rate; see text for details) are given in open circles, those obtained by method 2 (via the PL decay amplitude; see text for details) in closed disks. Solid lines connect symbols that belong to the same NR, i.e. the results of method 1 and 2. **a)** The correlation between the radiative lifetimes of the bright state A (the neutral exciton X^0) and the grey state B (the negative trion X^-). Radiative decay is faster in the grey state than in the bright state by a factor $1.89(\pm 0.26)$ (mean $\pm$ standard deviation). **b)** The correlation between the radiative and non-radiative lifetimes of the grey state. The resulting quantum efficiency of the grey state is $23(\pm 9)\%$.

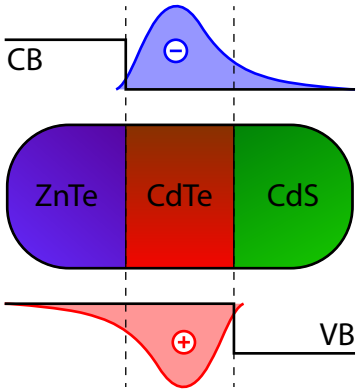

Figure S2 | The design of new colloidal systems with reduced Auger losses. A colloidal ZnTe/CdTe/CdS NR with a central CdTe region, and the two opposite tipis composed of ZnTe and CdS promises to possess suppressed Auger recombination in all excitonic states (X^-, X^+, and X_2). The band alignment (black solid lines) is such [1] that Coulomb attraction results in electron-hole overlap in the central CdTe part, hence efficient radiative recombination. At the same time, partial delocalization of both electron (into the CdS tip) and hole (into the ZnTe tip) leads to suppressed Auger recombination in all excitonic states. In addition, as for our NRs, partial delocalization will also lead to slower radiative rates than predicted by statistical scaling relations. Moreover, the biexciton will be repulsive, which is good for lasing applications.

SUPPLEMENTARY DISCUSSION 1 | QUENCHING OF BIEXCITON EMISSION

From photon-photon correlation $g^{(2)}$ plots (Fig. 1a inset, and panels a in the Supplementary Data) one can determine the quantum efficiency of the biexciton state X_2. Nair *et al.* [2] have shown that, in the limit of low excitation rates, the height of the zero-delay peak in a normalized $g^{(2)}$ plot is equal to ratio of X_2 quantum efficiency to X^0 quantum efficiency. For our NRs a zero-delay peak cannot be distinguished, hence X_2 emission is completely quenched. Clearly, the biexciton can still effectively decay via a non-radiative (Auger) pathway although we have seen that for the negative trion Auger decay is suppressed. The difference in Auger recombination rates of trion and biexciton has been observed and discussed before for the case of thick-shell CdSe/CdS QDs [3, 4], and is a consequence of the asymmetric confinement of CB electrons and valence band (VB) holes. The 'negative trion Auger pathway' in which a remaining electron accepts the recombination energy, is suppressed as evident from the high X^- quantum efficiency in our NRs. Non-radiative decay of X_2, however, can still be very fast via the 'positive trion Auger pathway', in which a remaining hole is the acceptor carrier. Indeed, the positive trion pathway is expected to be efficient in our NRs, since holes experience a hard confinement potential due to a large VB offset.

SUPPLEMENTARY DISCUSSION 2 | ESTIMATION OF RADIATIVE AND NON-RADIATIVE DECAY CONSTANTS

For reliable estimates of radiative and non-radiative contributions the excitation rate of the emitter must be roughly the same for each state. We have chosen our excitation wavelength (532 nm; 2.34 eV) such that this condition is fulfilled to within an estimated $\pm 10\%$. Two effects must be prevented as much as possible. (1) First, there may be differences between the absorption spectra of the charged and the uncharged state of the NR, due to orbital filling and Stark effects. Transient absorption measurements on ensembles of excited CdSe/CdS NRs [5, 6] and CdSe/CdS thick-shell QDs [7] revealed reduced absorption compared to ground-state emitters over a wide range of photon energies, ranging from the band-edge up to the blue. At the excitation wavelength we use, photoinduced absorption changes are relatively small: $\pm 10\%$, as measured for CdSe/CdS NRs similar to ours [5]. (2) Secondly, using non-resonant excitation results in hot carriers that cool to the bottom of the CB (electrons) or the top of the VB (holes) with an efficiency that may be $< 100\%$ and dependent on the presence of extra charges. Indeed, hot carrier trapping and/or ejection has been measured in PbSe QDs [8, 9], and CdSe/CdS QDs [10]. In our experiments we excite sufficiently near the band-edge of CdSe that we expect an exciton cooling efficiency close to unity. Considering the above we conclude that potential variations in the excitation rate of different states cause an estimated uncertainty of 10% in our estimates of radiative and non-radiative decay rates.

The two methods employed to estimate radiative and non-radiative decay contributions would yield the exact same result for a perfectly single-exponential PL decay curve, and in the absence of background noise. In Fig. 3a we see, however, that the radiative lifetimes of state B obtained by method 1 (via the photon count rates; open circles) are generally shorter by 10–20% than those obtained by method 2 (via the PL decay amplitude; closed circles). This discrepancy is due to time bins assigned to state B but in which one or more rapid B $\leftrightarrow$ A switching events happen. Hence, some photon counts originating from state A are assigned to state B. The apparent photon count rate of state B is slightly increased, since $M_{\mathrm{A}} > M_{\mathrm{B}}$. At the same time, as visible in Fig. 2a and panels c of the Supplementary Data, a weak long lifetime component ($\tau_{\mathrm{A}} > \tau_{\mathrm{B}}$) with low amplitude ($A_{\mathrm{A}} < A_{\mathrm{B}}$) appears in the PL decay curve of state B, so the apparent PL decay amplitude of state B decreases. As a result, method 1 (via the photon count rate) overestimates the radiative decay rate of state B, whereas method 2 (via the PL decay amplitude) underestimates it.

Supplementary Figure S1 shows that the trends observed in Figure 3 of the main text are robust to conservative assumptions of $\eta_{\mathrm{A}} = 0.75$ and a 20% lower excitation rate of state B compared to state A, rather than $\eta_{\mathrm{A}} = 1$ and equal excitation rates. Still we obtain a negative trion (state B) quantum efficiency of $23(\pm 9)\%$ and a radiative decay rate faster than for the neutral exciton (state A) by a factor $1.89(\pm 0.26)$.

SUPPLEMENTARY DISCUSSION 3 | THE TRANSITION ENERGIES

The differences in transition energy simulated for the X^0, X^-, and X^+ states (Fig. 4b) can already be understood qualitatively in terms of electron delocalization. To this end we write the transition energies as

$$\Delta E_{X^0} = E^{(0)} - J_{eh} \tag{S1}$$

$$\Delta E_{X^-} = E^{(0)} - 2J_{eh} + J_{ee} \tag{S2}$$

$$\Delta E_{X^+} = E^{(0)} - 2J_{eh} + J_{hh} \tag{S3}$$

where $E^{(0)}$ is the zeroth-order transition energy not including electron-hole interactions, i.e. only containing the band gap energy and electron and hole confinement energies. The terms J_{ij} denote the absolute value of the Coulomb interaction energy between carriers i and j. The value of a Coulomb term J_{ij} scales with the average of the inverse distance between carriers i and j. Since the electron wavefunctions are more extended than the hole wavefunctions, $J_{ee} < J_{eh} < J_{hh}$, i.e. electron-electron repulsion is weaker than electron-hole attraction which in turn is weaker than hole-hole repulsion. Therefore we find in Fig. 4b that in order of increasing transition energy $\Delta E_{X^-} < \Delta E_{X^0} < \Delta E_{X^+}$.

Previous spectral studies of single CdSe/CdS nanocrystals at room temperature [11–13] have not presented any indication for emission wavelength blinking as we observe it (Fig. 1c). The difference with our observation presumably stems from the long integration times used previously (1–3 s/frame) and a very low trion quantum efficiency. Montiel and Yang [14] have reported a correlation between emission intensity and wavelength for single CdSe/ZnS QDs, however not from direct spectral measurements but using a pair of band-pass filters

and point detectors. On the other hand, there are clear reports of emission wavelength blinking of single CdSe/ZnS nanocrystals at helium temperatures [15, 16], ascribed to exciton-trion switching. In these studies only spectral (no PL decay) measurements were performed, with time resolutions of $100\ \mathrm{ms}$ [15] and $1\ \mathrm{s}$ [16]. The separation between the narrow emission lines for the exciton and the trion is 10–22 meV in Ref. 15 and $< 10\ \mathrm{meV}$ in Ref. 16, in line with our results obtained at room temperature and at a higher time resolution.

SUPPLEMENTARY METHODS | THE EFFECTIVE MASS CALCULATIONS

We performed quantum-mechanical effective-mass calculations [17] to obtain estimations for the transition energies and radiative decay rates of the neutral exciton, and positive and negative trions in our NRs. Schrödinger's equation was solved using the finite element routine of COMSOL Multiphysics v4.1. We modelled a NR as a spherical CdSe core of $3.2\ \mathrm{nm}$ diameter, embedded in a cylindrical CdS rod of $5.6\ \mathrm{nm}$ diameter and $21\ \mathrm{nm}$ length with the centre of the core at $5\ \mathrm{nm}$ from one end of the rod (Fig. 4a). We calculated five different states of the NR: (A) the 1h-state, (B) the 1e-state, (C) the 1e1h-state (= exciton X^0), (D) the 1e2h-state (= positive trion X^+), and (E) the 2e1h-state (= negative trion X^-).

A. The 1h-state

Because of the strong confinement and large VB offset between CdS and CdSe, we always modelled the hole as a particle-in-a-spherical-box with infinite potential walls:

$$\left[-\frac{\hbar^2}{2m_h^*}\nabla^2 + V_{\mathrm{vb}}(\mathbf{r})\right]\psi_h(\mathbf{r}) = E_h\psi_h(\mathbf{r}), \tag{S4}$$

where we took $m_h^* = 0.45m_0$ [24] for the hole effective mass in CdSe, and approximated the top of the VB as an infinite potential well

$$V_{\mathrm{vb}}(\mathbf{r}) = \begin{cases} 0 & ; \ \mathbf{r} \in \text{CdSe} \\ \infty & ; \ \mathbf{r} \in \text{elsewhere} \end{cases} \tag{S5}$$

The ground state ψ_h and corresponding energy E_h are directly the solutions for the 1h-state of the NR. In a next step we calculated the Coulomb potential $\phi_h(\mathbf{r})$ due to the hole ground state ψ_h by solving Poisson's equation

$$\nabla^2\phi_h(\mathbf{r}) = \frac{e\,|\psi_h(\mathbf{r})|^2}{\epsilon\epsilon_0}, \tag{S6}$$

where we took a dielectric constant of $\epsilon = 10$ in all space. To ensure that ϕ_h approach zero at infinity, we imposed a boundary condition on a spherical surface far from the nanorod:

$$\phi_h(|\mathbf{r} - \mathbf{r}_0| = 250\ \mathrm{nm}) = \frac{e}{4\pi\epsilon\epsilon_0} \times \frac{1}{250\ \mathrm{nm}} = 0.576\ \mathrm{mV}, \tag{S7}$$

with $\mathbf{r}_0$ the center of the CdSe core.

B. The 1e-state

The electron wavefunctions and energies for the 1e-state are calculated by solving

$$\left[\frac{-\hbar^2}{2m_e^*(\mathbf{r})}\nabla^2 + V_{\mathrm{cb}}(\mathbf{r})\right]\psi_e(\mathbf{r}) = E_e\psi_e(\mathbf{r}), \tag{S8}$$

where the electron effective mass [24]

$$m_e^*(\mathbf{r}) = \begin{cases} 0.13m_0 & ; \ \mathbf{r} \in \text{CdSe} \\ 0.21m_0 & ; \ \mathbf{r} \in \text{elsewhere} \end{cases} \tag{S9}$$

and the bottom of the conduction band

$$V_{\mathrm{cb}}(\mathbf{r}) = \begin{cases} -V_{\mathrm{cbo}} & ; \ \mathbf{r} \in \text{CdSe} \\ 0 & ; \ \mathbf{r} \in \text{CdS} \\ \infty & ; \ \mathbf{r} \in \text{elsewhere} \end{cases} \tag{S10}$$

Here we assumed an infinite potential outside the rod. The CB offset between CdSe and CdS is not well known. Different values between $0\ \mathrm{meV}$ and $300\ \mathrm{meV}$ are given in literature [18–20]. Therefore, we performed our calculations for a range of values for the CB offset of $V_{\mathrm{cbo}} = \{0, 50, 100, 200, 300\}\ \mathrm{meV}$.

C. The 1e1h-state (= neutral exciton X^0)

The exciton (1e1h) wavefunction is written as

$$\Psi_{X^0}(\mathbf{r}_e, \mathbf{r}_h) = \psi_{e,X^0}(\mathbf{r}_e)\psi_h(\mathbf{r}_h). \tag{S11}$$

Here we assume that the hole part ψ_h is equal to the wavefunction of the 1h-state, since the shape is determined by strong confinement. On the other hand, we allow the electron part ψ_{e,X^0} to adjust (compared to the 1e-state ψ_e) under the influence of Coulomb attraction from the hole. We solve

$$\left[\frac{-\hbar^2}{2m_e^*(\mathbf{r})}\nabla^2 + V_{\text{cb}}(\mathbf{r}) - e\phi_h(\mathbf{r})\right]\psi_{e,X^0}(\mathbf{r}) = E_{e,X^0}\psi_{e,X^0}(\mathbf{r}) \tag{S12}$$

The total energy of the exciton is then given by

$$E_{X^0} = E_{e,X^0} + E_h \tag{S13}$$

D. The 1e2h-state (= positive trion X^+)

The positive trion (1e2h) ground state is written as

$$\Psi_{X^+}(\mathbf{r}_e, \mathbf{r}_{h1}, \mathbf{r}_{h2}) = \frac{1}{\sqrt{2}}\psi_{e,X^+}(\mathbf{r}_e)\left[\psi_h(\mathbf{r}_{h1})\overline{\psi_h}(\mathbf{r}_{h2}) - \overline{\psi_h}(\mathbf{r}_{h1})\psi_h(\mathbf{r}_{h2})\right], \tag{S14}$$

where ψ_h and $\overline{\psi_h}$ denote two different hole spin projections. Again, we assume the hole part ψ_h equal to the wavefunction of the 1h-state, and allow the electron part ψ_{e,X^+} to adjust under the influence of Coulomb attraction from the two holes. We solve

$$\left[\frac{-\hbar^2}{2m_e^*(\mathbf{r})}\nabla^2 + V_{\text{cb}}(\mathbf{r}) - 2e\phi_h(\mathbf{r})\right]\psi_{e,X^+}(\mathbf{r}) = E_{e,X^+}\psi_{e,X^+}(\mathbf{r}) \tag{S15}$$

The total energy of the positive trion is then given by

$$E_{X^+} = E_{e,X^+} + 2E_h + J_{hh}, \tag{S16}$$

where

$$J_{hh} = \int \psi_h(\mathbf{r})e\phi_h(\mathbf{r})\psi_h(\mathbf{r})\,\mathrm{d}^3\mathbf{r} \tag{S17}$$

is the hole-hole Coulomb repulsion energy. The value for $J_{hh} = 160.682\ \text{meV}$ obtained from the COMSOL calculations lies within 0.05% of the value of the analytical Coulomb integral $J_{hh} = \int |\psi(\mathbf{r})|^2 \frac{e^2}{4\pi\epsilon\epsilon_0|\mathbf{r}-\mathbf{r}'|}|\psi(\mathbf{r}')|^2\,\mathrm{d}^3\mathbf{r}\,\mathrm{d}^3\mathbf{r}'$ evaluated in Wolfram Mathematica using the analytical particle-in-a- spherical-box ground state for the hole wavefunction $\psi(\mathbf{r})$.

E. The 2e1h-state (= negative trion X^-)

The negative trion (2e1h) ground state (with paired electron spins) is written as

$$\Psi_{X^-}(\mathbf{r}_{e1}, \mathbf{r}_{e2}, \mathbf{r}_h) = \frac{1}{\sqrt{2}}\left[\psi_{e,X^-}(\mathbf{r}_{e1})\overline{\psi_{e,X^-}}(\mathbf{r}_{e2}) - \overline{\psi_{e,X^-}}(\mathbf{r}_{e1})\psi_{e,X^-}(\mathbf{r}_{e2})\right]\psi_h(\mathbf{r}_h) \tag{S18}$$

Again, we assume the hole part ψ_h equal to the wavefunction of the 1h-state, and allow the wavefunction ψ_{e,X^-} of the two electrons to adjust under the influence of Coulomb attraction from the hole and mutual Coulomb repulsion. We solve for ψ_{e,X^-} using an iterative procedure. We use the electron wavefunction ψ^i_{e,X^-} from iteration step i to obtain the Coulomb potential $\phi^i_e(\mathbf{r})$ using the Poisson equation:

$$\nabla^2\phi^i_e(\mathbf{r}) = \frac{e\left|\psi^i_e(\mathbf{r})\right|^2}{\epsilon\epsilon_0}, \tag{S19}$$

with the dielectric constant and the boundary condition as before for ϕ_h. Then we solve the electron wavefunction ψ^{i+1}_{e,X^-} of the next iterative step from the Schrödinger equation

$$\left[\frac{-\hbar^2}{2m_e^*(\mathbf{r})}\nabla^2 + V_{\text{cb}}(\mathbf{r}) - e\phi_h(\mathbf{r}) + e\phi^i_e(\mathbf{r})\right]\psi^{i+1}_{e,X^-}(\mathbf{r}) = E^{i+1}_{e,X^-}\psi^{i+1}_{e,X^-}(\mathbf{r}) \tag{S20}$$

This procedure is repeated until we obtain a self-consistent electron wavefunction and energy. Typically after less than 10 iterative steps the energy E_{e,X^-} has converged to within $1\ \text{meV}$. For the initial guess of the electron wavefunction we use the electron wavefunction of the neutral exciton state $\psi^1_{e,X^-} = \psi_{e,X^0}$. The energy of the negative trion is given by

$$E_{X^-} = 2E_{e,X^-} + E_h - J_{ee} \tag{S21}$$

where the term

$$J_{ee} = \int \psi_{e,X^-}(\mathbf{r})e\phi_{e,X^-}(\mathbf{r})\psi_{e,X^-}(\mathbf{r})\,\mathrm{d}^3\mathbf{r} \tag{S22}$$

is subtracted to avoid double counting of the electron-electron repulsion.

F. Radiative transition rates

Radiative transition rates can now be obtained from the electron-hole overlap integrals [21]:

$$\tau_{\mathrm{r},X^0}^{-1} = \frac{1}{2} C \left| \int \psi_{e,X^0}(\mathbf{r}) \psi_h(\mathbf{r}) \, \mathrm{d}^3\mathbf{r} \right|^2 \tag{S23}$$

$$\tau_{\mathrm{r},X^\pm}^{-1} = C \left| \int \psi_{e,X^\pm}(\mathbf{r}) \psi_h(\mathbf{r}) \, \mathrm{d}^3\mathbf{r} \right|^2 \tag{S24}$$

The factor $\frac{1}{2}$ in the expression for $\tau_{\mathrm{r},X^0}^{-1}$ accounts for the fact that only one spin-projection of the electron allows recombination with the hole (or equivalently, there is 50% thermal population of dark exciton states [21, 22]). The prefactor $C = \frac{4e^2 \omega n P^2 |\chi|^2}{9 \times 4\pi\epsilon_0 m_0^2 c^3 \hbar} = 1/(8.7 \text{ ns})$, where n is the refractive index of the environment ($n = 1.5$ for glass), P is the Kane interband matrix element ($2P^2/m_0 = 19.0$ eV for CdSe [21]), and χ is a local field factor accounting for the local density of optical states on the position of the NR. We take $\chi = \frac{3n^2}{2n^2 + n_{\mathrm{CdSe}}^2} = 0.685$, ignoring the asymmetric shape of the NR, and the presence of air above the sample. The approximate value for χ only affects the absolute values obtained for the radiative decay rates, and do not lead to different ratios of the rates of X^0, X^- and X^+.

G. Transition energies

The transition energies of X^0, X^- and X^+ can now be determined from the energies of the states calculated above, and the band gap energy. In the calculations we took the bottom of the CB in CdS as $E = 0$ for the electrons, and the top of the VB in CdSe as $E = 0$ for the holes. Then the transition energies are given by

$$\Delta E_{X^0} = E_{X^0} + E_g + V_{\mathrm{cbo}} \tag{S25}$$

$$\Delta E_{X^+} = E_{X^+} - E_h + E_g + V_{\mathrm{cbo}} \tag{S26}$$

$$\Delta E_{X^-} = E_{X^-} - \left[\sum_i E_e^i \left| \int \psi_{e,X^-}(\mathbf{r}) \psi_e^i(\mathbf{r}) \, \mathrm{d}^3\mathbf{r} \right|^2 \right] + E_g + V_{\mathrm{cbo}} \tag{S27}$$

where the summation over 1e-states ψ_e^i accounts for a finite probability for radiative decay of the negative trion to excited single-electron states (compare Ref. 23), and $E_g = 1.7$ eV is the band gap energy of CdSe. The single-electron energy states are closely spaced in energy (typical separation 25 meV), so that separate lines are not distinguished in the emission spectra which are already broadened by phonon coupling.

The absolute values for transition energy that we calculate, are some 200 meV higher than those obtained experimentally. The discrepancy can be attributed to the uncertainty in the exact positions of CB and VB extremes, and an overestimation of the hole confinement energy (due to the approximation of infinite potential outside the CdSe core). Fortunately, however, these parameters do not affect the differences in transition energy of X^0, X^- and X^+ that we required in the main text for our assignment of the sign of the trion charge.

SUPPLEMENTARY DATA | OVERVIEW OF THE RESULTS FOR ALL 18 SINGLE NRS EXAMINED

The results for all 18 single NRs examined are presented on the following pages. We present an overview of our entire data set here so that the reader can properly judge the similarities and variations between the different individual NRs. Careful inspection of the data will reveal features (e.g. an apparent correlation between the quality of the Poissonian fit to the intensity histogram and the single exponential character of the PL decay curve) that are beyond the scope of this article to fully investigate and discuss. However, we do hope that such features can inspire future research.

Each of the 18 panels is arranged as follows. **a)** The photon-photon correlation plot, proving the observation of a single NR. **b)** The fluorescence-lifetime-intensity-distribution (FLID) and the corresponding intensity histogram. For computational advantages we use the parameter of average lifetime $\langle \tau \rangle = \sum N_i t_i / \sum N_i$ (where N_i is the number of photon counts at delay time t_i) in these FLIDs, rather than fitted lifetime as in the FLID presented in the main text. The dashed white boxes indicate the different states identified. Red lines in the intensity histogram are fits to Poissonian distributions (obtained with a least-squares method). **c)** State-resolved PL decay curves, obtained by averaging data from time bins highlighted in **b**, for state A (green), B (red), and C/D (blue). Solid black lines are single exponential fits. **d)** The emission-wavelength-intensity-distribution (EWID) and the corresponding intensity histogram. Again, dashed white boxes indicate the different states identified. **e)** State-resolved emission spectra, obtained by averaging data from spectral frames highlighted in **d**, for state A (green), B (red), and C (blue). Solid lines are fits to a series of phonon replicas. The table at the top-right summarizes the photon count rate M, PL decay amplitude A, lifetime τ, and zero-phonon emission peak energy E_0 for the states identified for the NR.

We remark that in many FLIDs the different states are still distinct, but they appear connected by "smearing". This effect has been discussed before by Galland *et al.* [25], and can be ascribed by rapid charging/discharging events that occur on a time-scale faster than a time bin (10 ms). Time bins in which the NR switches between state A and B, result in weighted average photon count rates and average lifetimes.

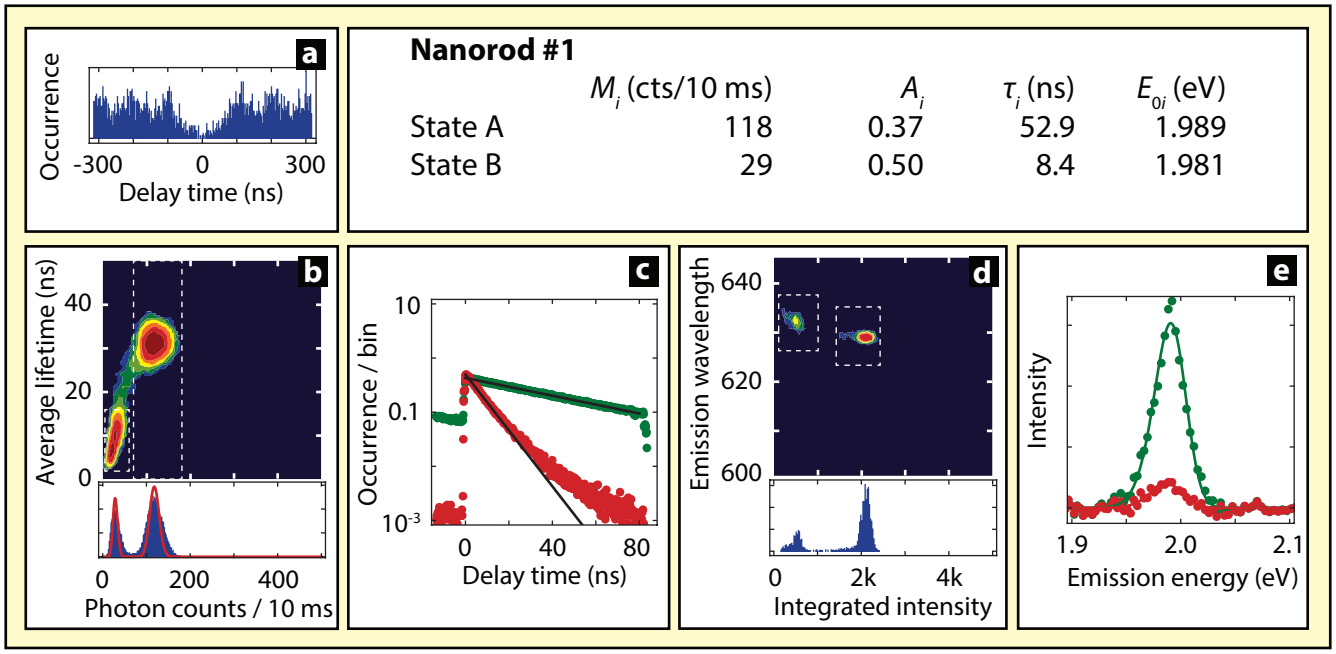

Figure S3 | The characteristics of nanorod #1.

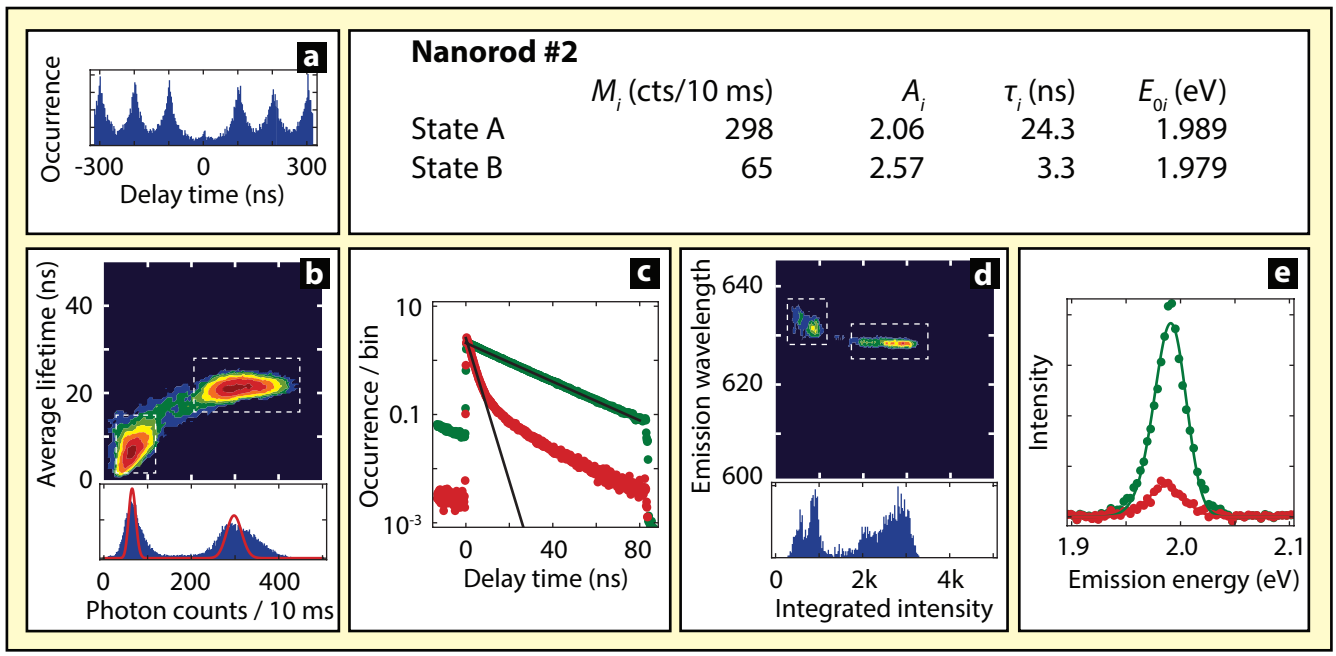

Figure S4 | The characteristics of nanorod #2.

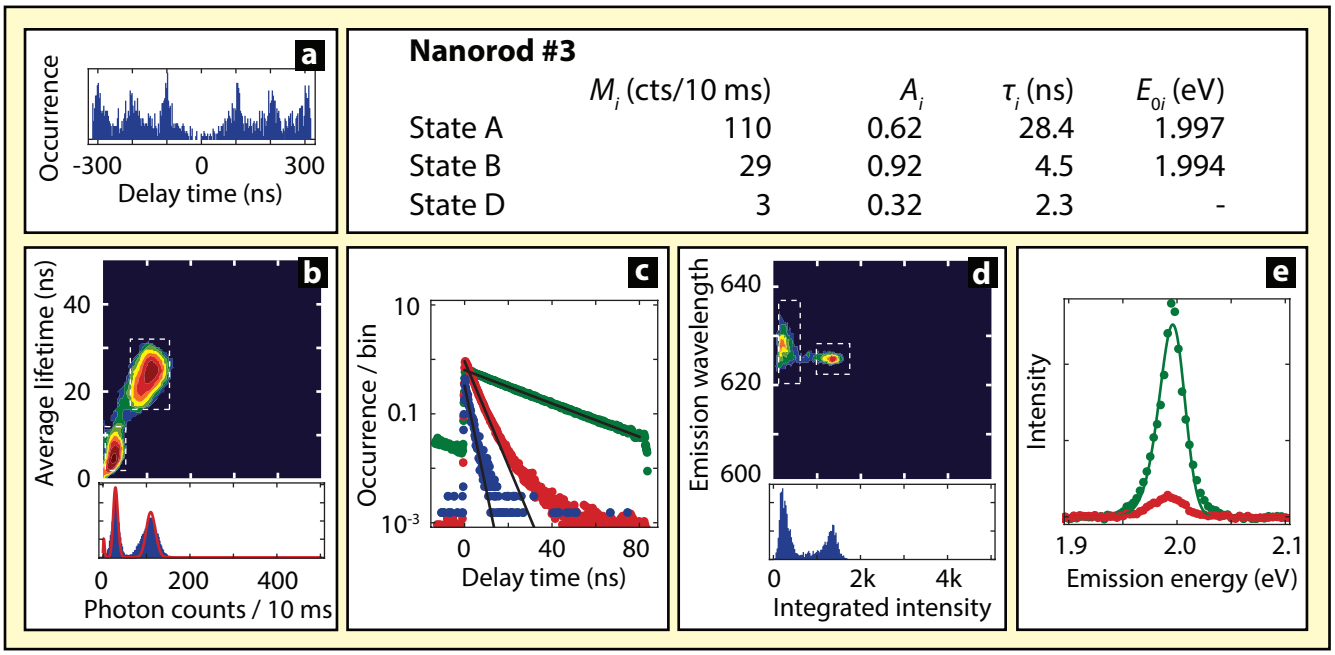

Figure S5 | The characteristics of nanorod #3.

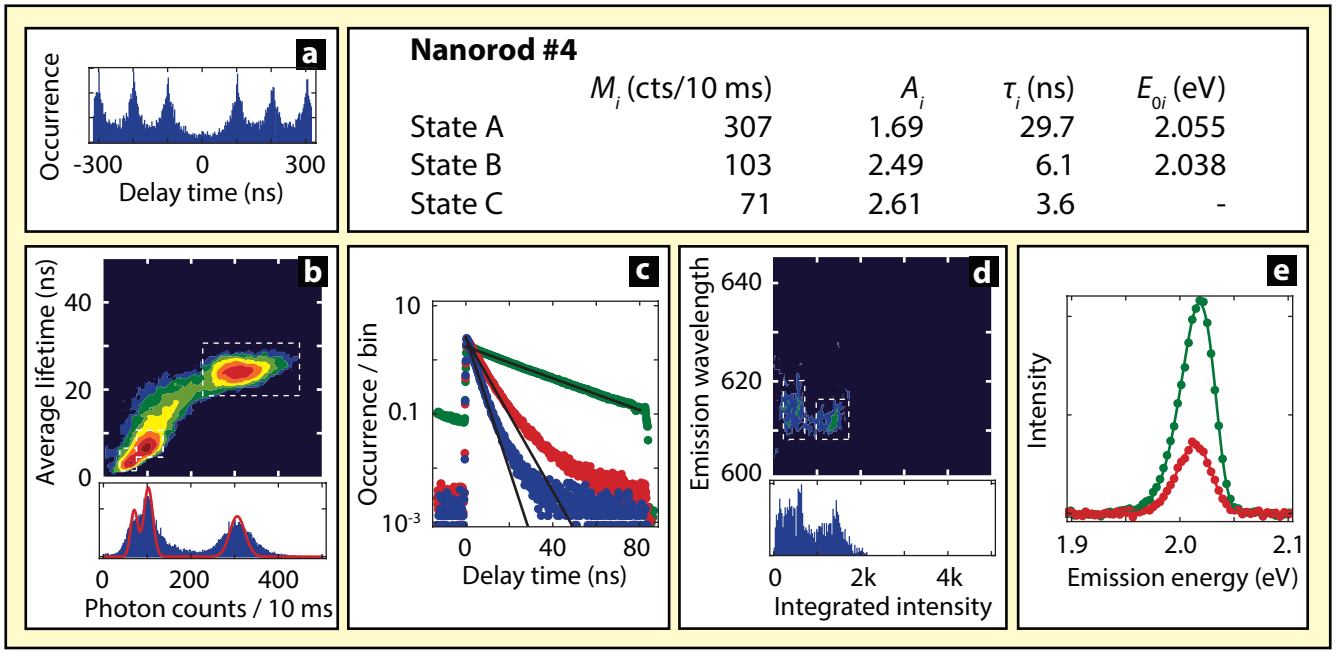

Figure S6 | The characteristics of nanorod #4.

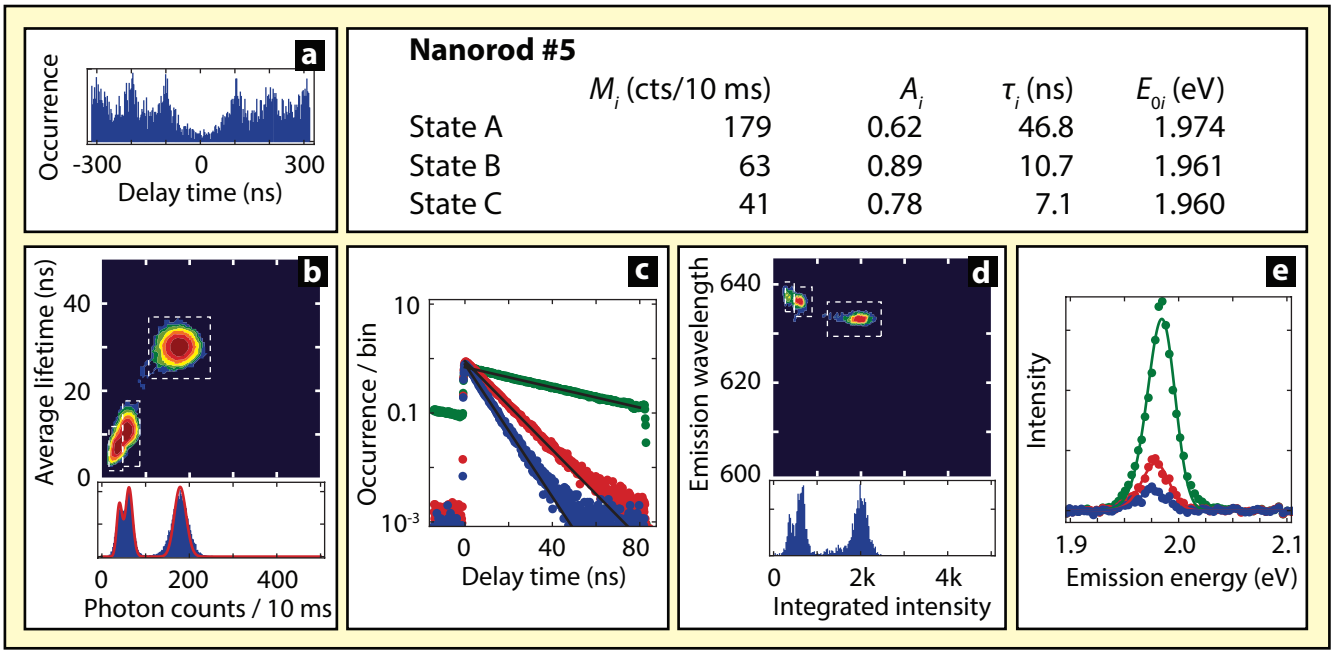

Figure S7 | The characteristics of nanorod #5.

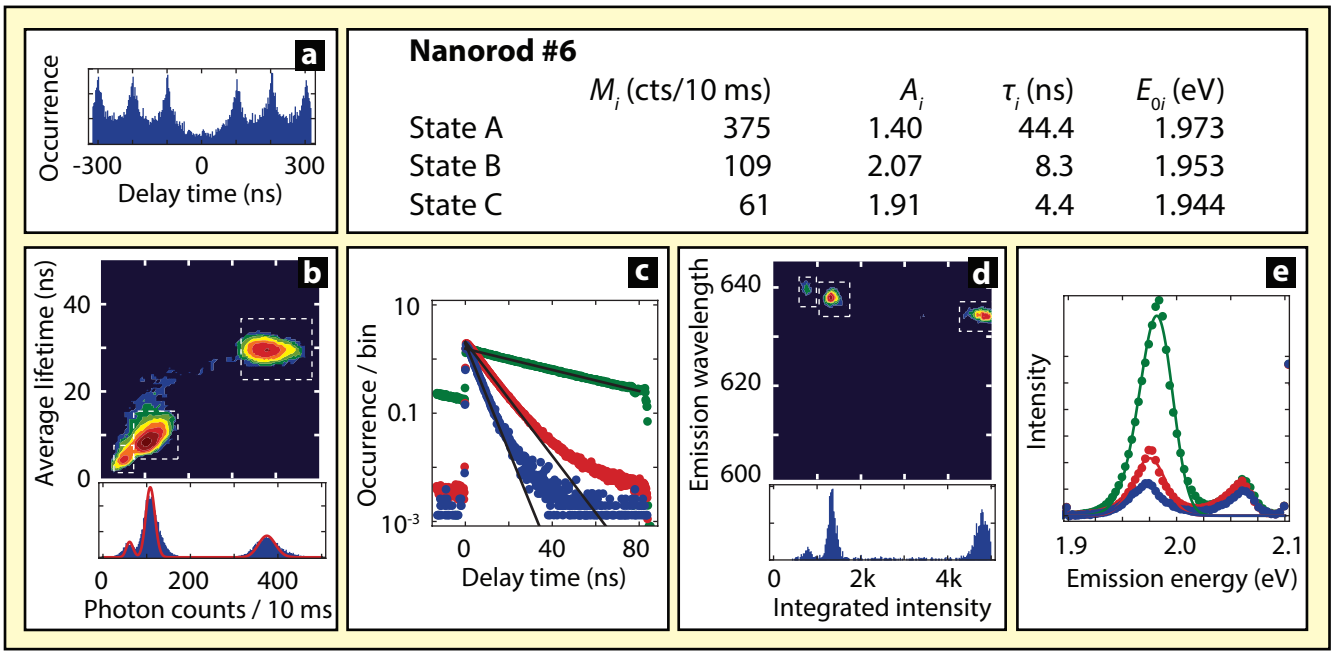

Figure S8 | The characteristics of nanorod #6.

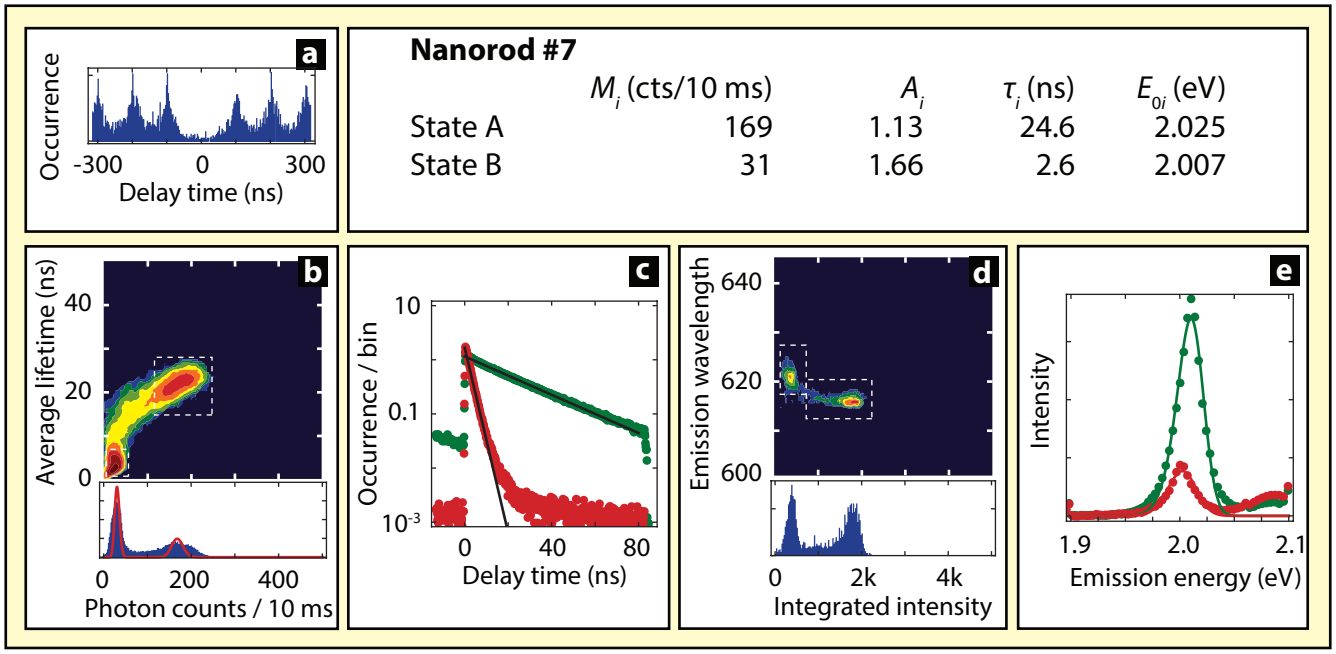

Figure S9 | The characteristics of nanorod #7.

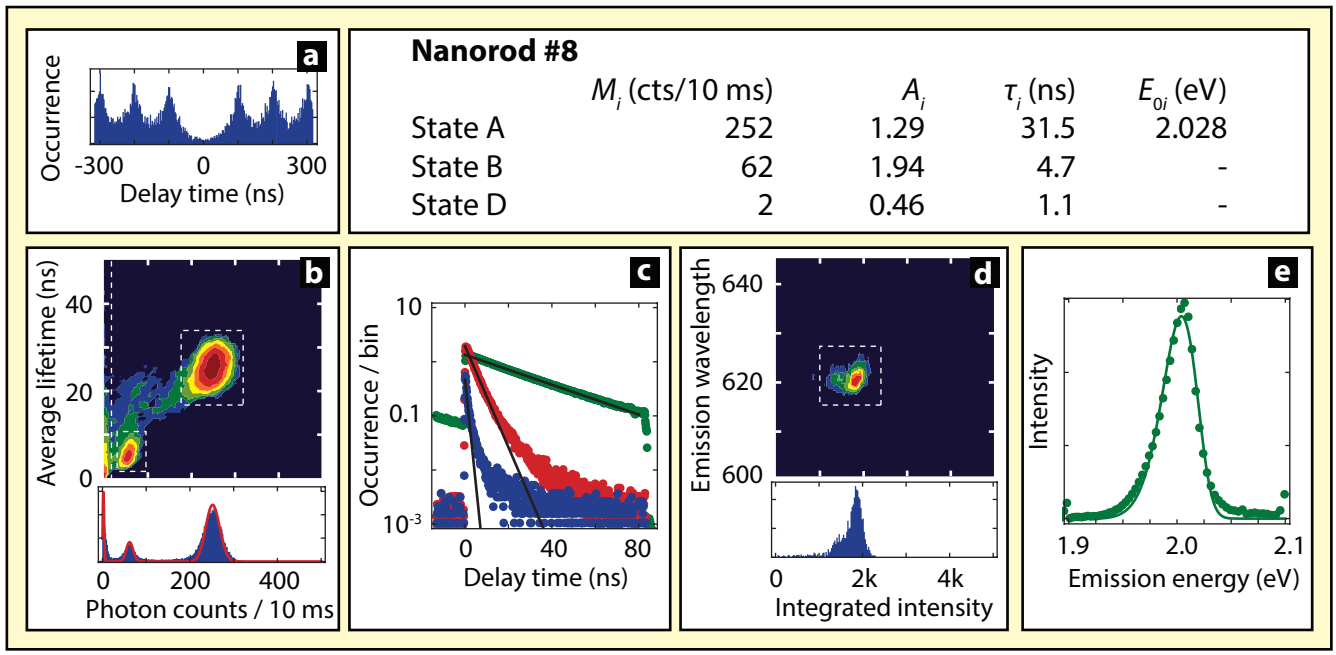

Figure S10 | The characteristics of nanorod #8.

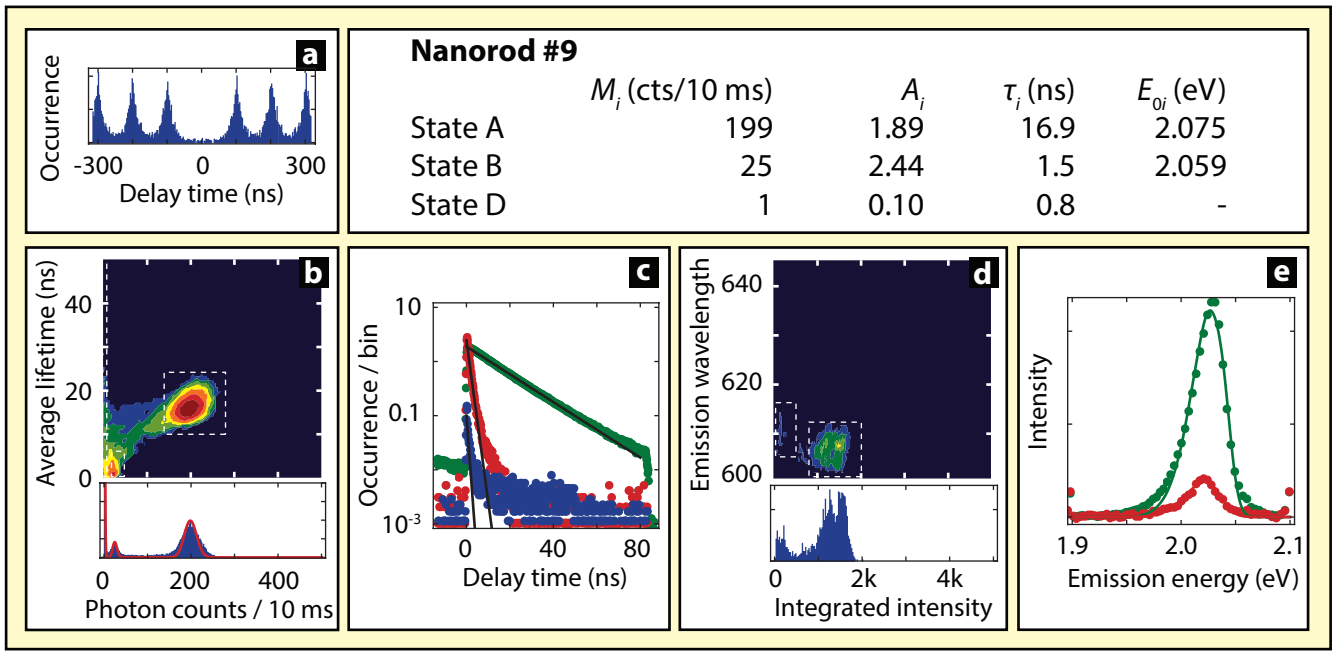

Figure S11 | The characteristics of nanorod #9.

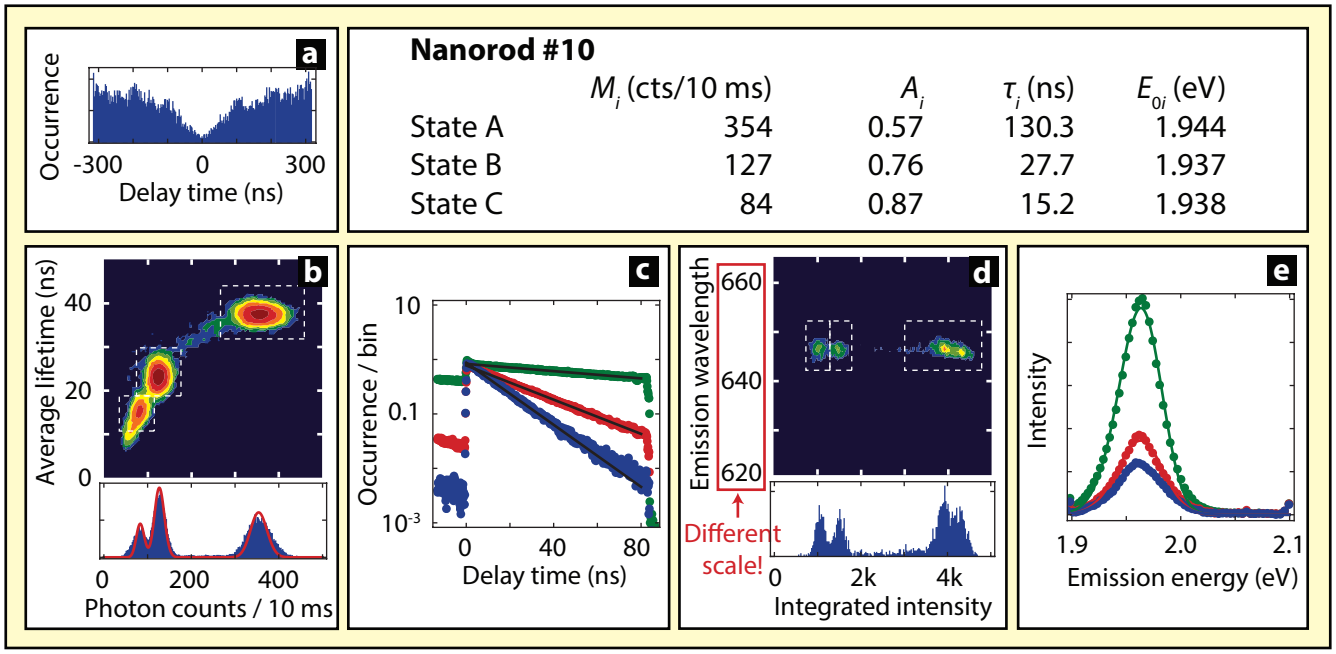

Figure S12 | The characteristics of nanorod #10.

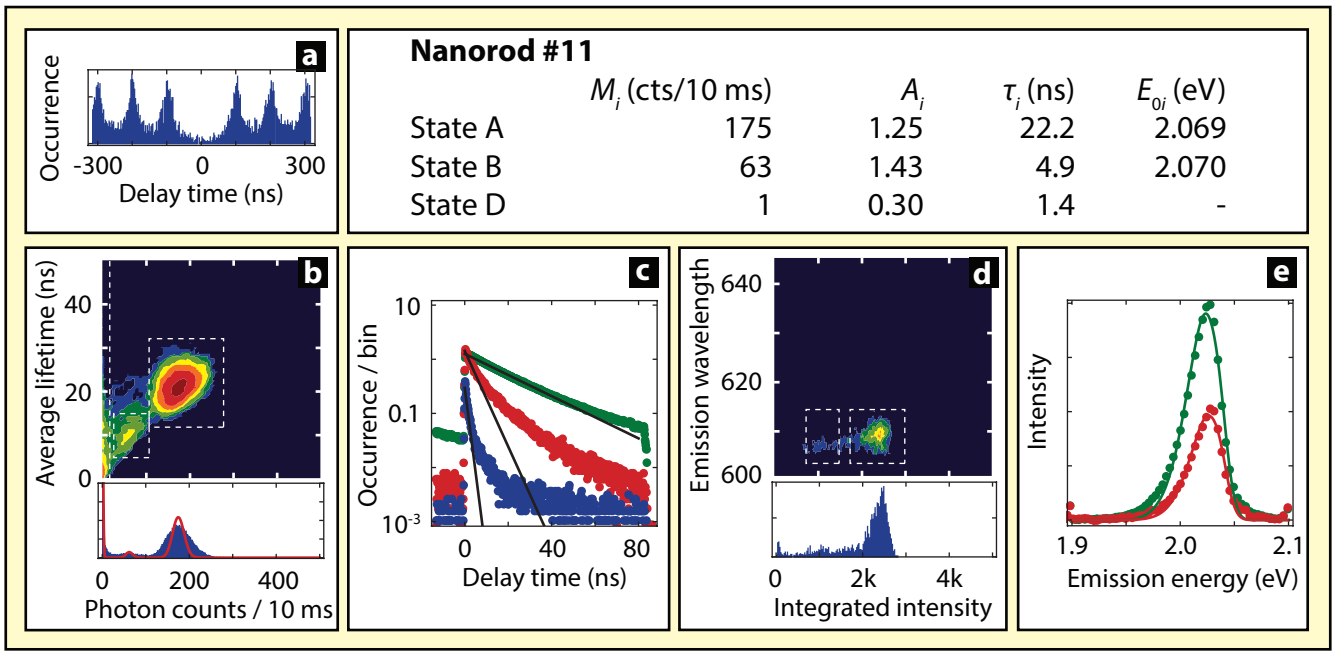

Figure S13 | The characteristics of nanorod #11.

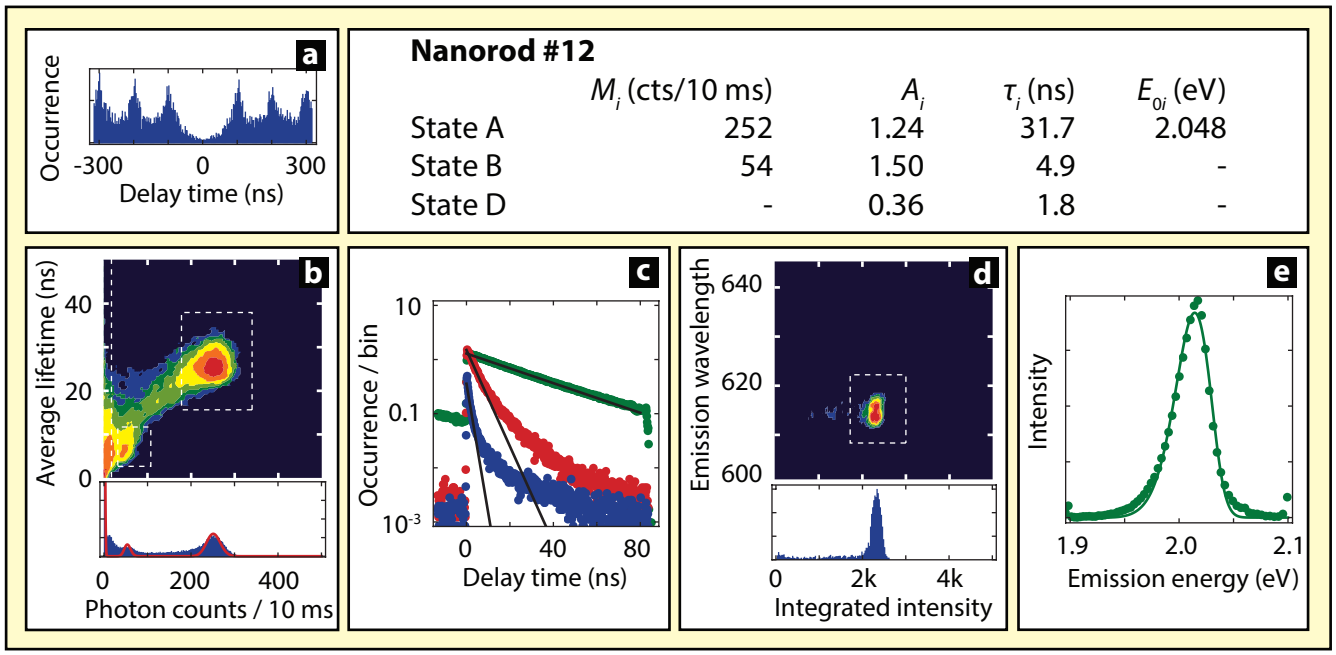

Figure S14 | The characteristics of nanorod #12.

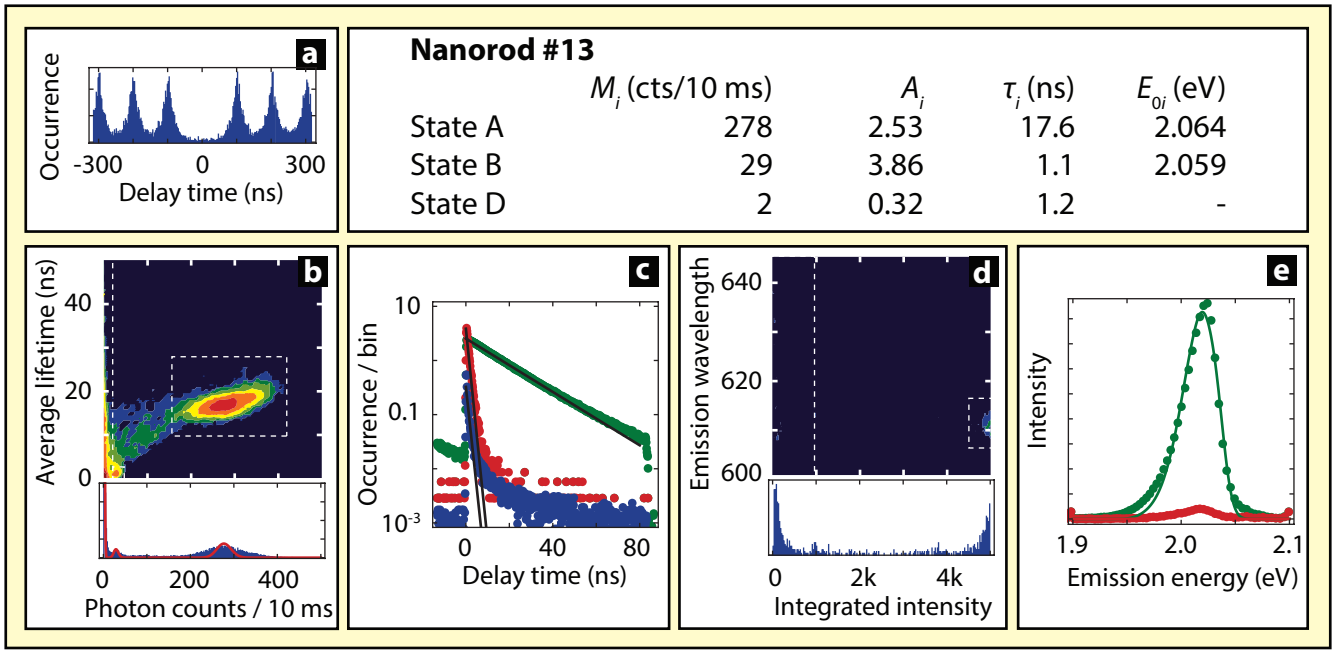

Figure S15 | The characteristics of nanorod #13.

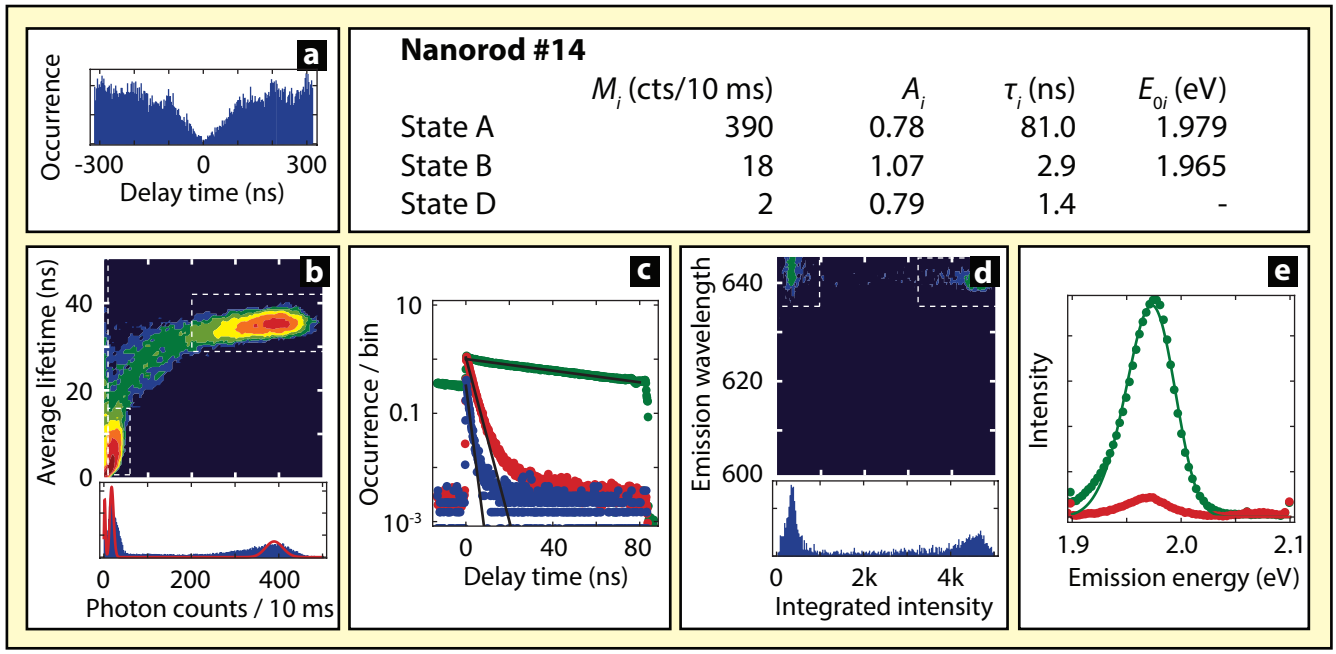

Figure S16 | The characteristics of nanorod #14.

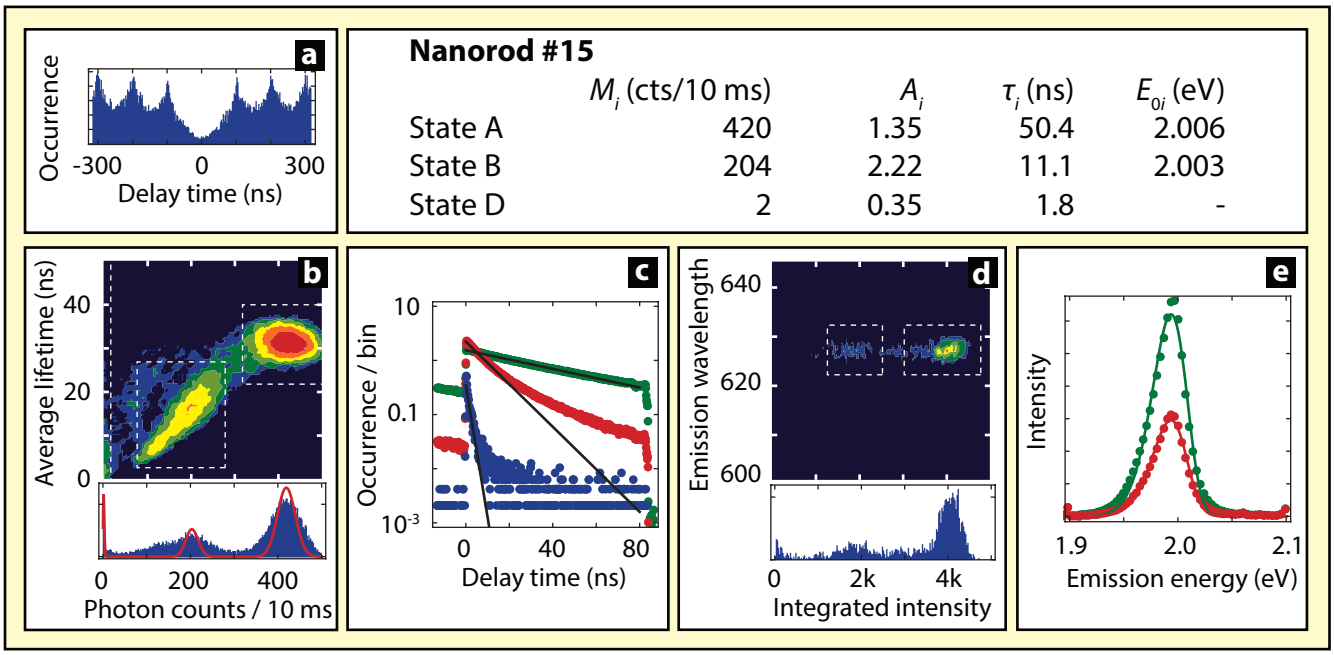

Figure S17 | The characteristics of nanorod #15.

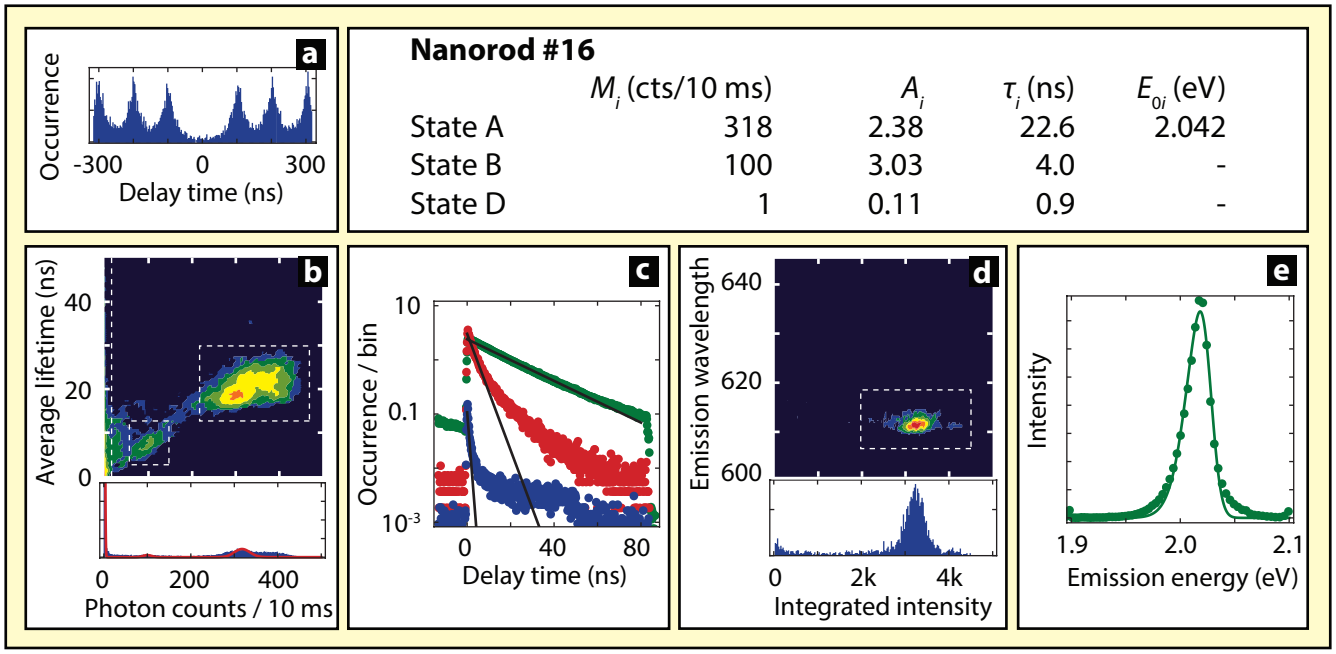

Figure S18 | The characteristics of nanorod #16.

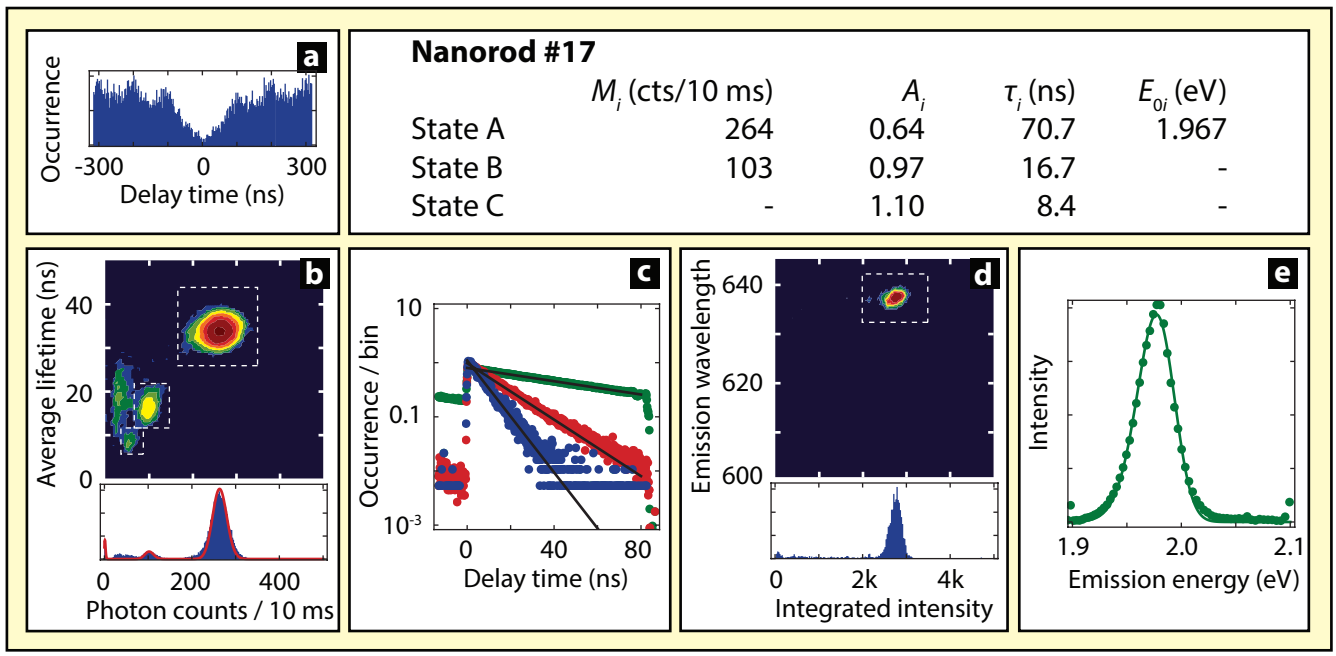

Figure S19 | The characteristics of nanorod #17.

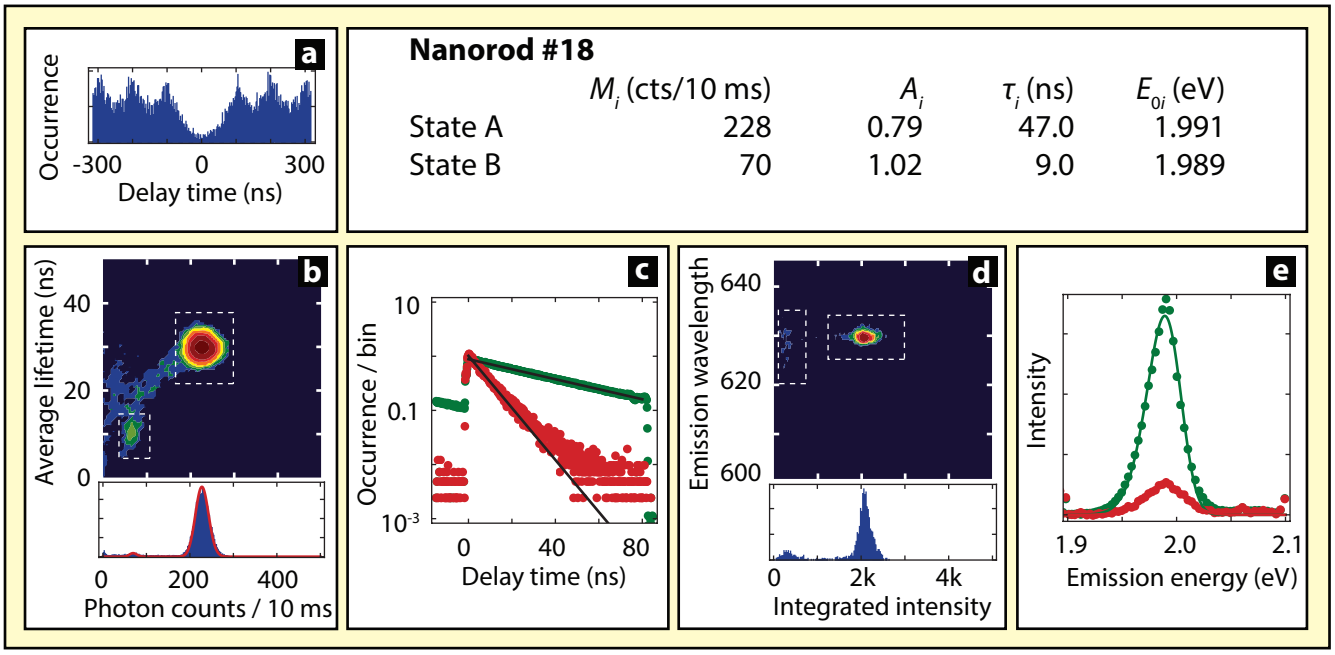

Figure S20 | The characteristics of nanorod #18.

REFERENCES

(1) De Mello Donegá, C. *Chem. Soc. Rev.* **2011**, *40*, 1512-1546.
(2) Nair, G.; Zhao, J.; Bawendi, M. G. *Nano Lett.* **2011**, *11*, 1136–1140.
(3) Malko, A. V.; Park, Y.-S.; Sampat, S.; Galland, C.; Vela, J.; Chen. Y.; Hollingsworth, J. A.; Klimov, V. I.; Htoon, H. *Nano Lett.* **2011**, *11*, 5213–5218.
(4) Galland, C.; Ghosh, Y.; Steinbrück, A.; Hollingsworth, J. A.; Htoon, H.; Klimov, V. I. *Nat. Commun.* **2012**, *3*, 908.
(5) Lupo, M. G.; Della Sala, F.; Carbone, L.; Zavelani-Rossi, M.; Fiore, A.; Lüer, L.; Polli, D.; Cingolani, R.; Manna, L.; Lanzani, G. *Nano Lett.* **2008**, *8*, 12, 4582–4587.
(6) Lupo, M. G.; Scotognella, F.; Zavelani-Rossi, M.; Lanzani, G.; Manna, L.; Tassone, F. *Phys. Chem. Chem. Phys.* **2012**, *14*, 7420–7426.
(7) Marceddu, M.; Saba, M.; Quochi, F.; Lai, A.; Huang, J.; Talapin, D. V.; Mura, A.; Bongiovanni, G. *Nanotechnology* **2012**, *23*, 015201.
(8) Padilha, L. A.; Robel, I.; Lee, D. C.; Nagpal, P.; Pietryga, J. M.; Klimov, V. I. *ACS Nano* **2011**, *5*, 6, 5045–5055.
(9) Tisdale, W. A.; Williams, K. J.; Trimp, B. A.; Norris, D. J.; Aydil, E. S.; Zhu, X.-Y. *Science* **2010**, *328*, 1543.
(10) Li, S.; Steigerwald, M. L.; Brus. L. E. *ACS Nano* **2009**, *3*, 5, 1267–1273.
(11) Müller, J.; Lupton, J. M.; Rogach, A. L.; Feldmann, J.; Talapin, D. V.; Weller, H. *Phys. Rev. Lett.* **2004**, *93*, 16, 167402.
(12) Müller, J.; Lupton, J. M.; Rogach, A. L.; Feldmann, J.; Talapin, D. V.; Weller, H. *Phys. Rev. B* **2005**, *72*, 205339.
(13) Gómez, D. E.; Van Embden, J.; Mulvaney, P. *Appl. Phys. Lett.* **2006**, *88*, 154106.
(14) Montiel, D.; Yang, H. *J. Phys. Chem. A* **2008**, *112*, 9352–9355.
(15) Shimizu, K. T.; Woo, W. K.; Fisher, B. R.; Eisler, H. J.; Bawendi, M. G. *Phys. Rev. Lett.* **2002**, *89*, 11, 117401.
(16) Fernée, M. J.; Littleton B. N.; Rubinsztein-Dunlop, H. *ACS Nano* **2009**, *3*, 11, 3762–3768.
(17) Delerue, C.; Lannoo, M. *Nanostructures – Theory and Modelling*, Springer-Verlag, Berlin, 2004
(18) Müller, J.; Lupton, J. M.; Lagoudakis, P. G.; Schindler, F.; Koeppe, R.; Rogach, A. L.; Feldmann J. *Nano Lett.* **2005**, *5*, 2044–2049.
(19) Steiner, D.; Dorfs, D.; Banin, U.; Della Sala, F.; Manna, L.; Millo, O. *Nano Lett.* **2008**, *8*, 2954–2958.
(20) Luo, Y.; Wang, L.-W. *ACS Nano* 2010, *4*, 1, 91–98.
(21) Shabaev, A.; Rodina, A. V.; Efros, Al. L. *Phys. Rev. B* **2012**, *86*, 205311.
(22) Efros, Al. L.; Rosen. M.; Kuno, M.; Nirmal, M.; Norris, D. J.; Bawendi, M. *Phys. Rev. B* **1996**, *54*, 7, 4843–4853.
(23) Wang, X.; Ren. X.; Kahen, K.; Hahn, M. A.; Rajeswaran, M.; Maccagnano-Zacher, S.; Silcox, J.; Cragg, G. E.; Efros, Al. L.; Krauss, T. D. *Nature* **2009**, *459*, 686–689.
(24) Brovelli, S.; Schaller, R. D.; Crooker, S. A.; García-Santamaría, F.; Chen, Y.; Viswanatha, R.; Hollingsworth, J. A.; Htoon, H.; Klimov, V. I. *Nat. Commun.* **2011**, *2*, 280.
(25) Galland, C.; Ghosh, Y.; Steinbrück, A.; Sykora, M.; Hollingsworth, J. A.; Klimov, V. I.; Htoon, H. *Nature* **2011**, *479*, 203–207.